

Hydrogeological Uncertainty Estimation with the Analytic Element Method

Maximilian Ramgraber¹ and Mario Schirmer²

¹Eawag - Swiss Federal Institute of Aquatic Science and Technology

²EAWAG

November 21, 2022

Abstract

Uncertainty estimation is an important part of practical hydrogeology. With most of the subsurface unobservable, attempts at system characterization will invariably be incomplete. Uncertainty estimation, then, must quantify the influence of unknown parameters, forcings, and structural deficiencies. In this endeavour, numerical modeling frameworks support an unparalleled degree of subsurface complexity and its associated uncertainty. When boundary uncertainty is concerned, however, the numerical framework can be restrictive. The interdependence of grid discretization and the enclosing boundaries make exploring uncertainties in their extent or nature difficult. The Analytic Element Method (AEM) may be an interesting complement, as it is computationally efficient, economic with its parameter count, and does not require enclosure through finite boundaries. These properties make AEM well-suited for comprehensive uncertainty estimation, particularly in data-scarce settings or exploratory studies. In this study, we explore the use of AEM for flow field uncertainty estimation, with a particular focus on boundary uncertainty. To induce versatile, uncertain regional flow more easily, we propose a new element based on conformal mapping. We then include this element in a simple Python-based AEM toolbox and benchmark it against MODFLOW. Coupling AEM with a Markov Chain Monte Carlo (MCMC) routine using adaptive proposals, we explore its use in a synthetic case study. We find that AEM permits efficient uncertainty estimation for groundwater flow fields, and its analytical nature readily permits continuing analyses which can support Lagrangian transport modelling or the placement of numerical model boundaries.

Hosted file

supporting_information_01.docx available at <https://authorea.com/users/528296/articles/596837-hydrogeological-uncertainty-estimation-with-the-analytic-element-method>

1 **Hydrogeological Uncertainty Estimation with the Analytic Element Method**

2 **M. Ramgraber^{1,2}, M. Schirmer^{1,2}**

3 ¹Department of Water Resources and Drinking Water, Eawag - Swiss Federal Institute of Aquatic Science and
4 Technology, Switzerland

5 ²Centre for Hydrogeology and Geothermics (CHYN), University of Neuchâtel, Switzerland

6

7 Corresponding author: *Maximilian Ramgraber* (max.ramgraber@eawag.ch).

8

9 **Key Points:**

- 10 • In this study, we explore the use of the Analytic Element Method (AEM) for
11 hydrogeological uncertainty estimation using a MCMC algorithm
- 12 • We include a flexible element based on conformal mapping for the influence of uncertain
13 regional flow in a simple Python-based AEM toolbox
- 14 • We find that AEM can be a useful tool for direct steady-state uncertainty estimation or
15 act as a support tool during model creation
16

17 **Abstract**

18 Uncertainty estimation is an important part of practical hydrogeology. With most of the
19 subsurface unobservable, attempts at system characterization will invariably be incomplete.
20 Uncertainty estimation, then, must quantify the influence of unknown parameters, forcings, and
21 structural deficiencies. In this endeavour, numerical modeling frameworks support an
22 unparalleled degree of subsurface complexity and its associated uncertainty. When boundary
23 uncertainty is concerned, however, the numerical framework can be restrictive. The
24 interdependence of grid discretization and the enclosing boundaries make exploring
25 uncertainties in their extent or nature difficult. The Analytic Element Method (AEM) may be an
26 interesting complement, as it is computationally efficient, economic with its parameter count,
27 and does not require enclosure through finite boundaries. These properties make AEM well-
28 suited for comprehensive uncertainty estimation, particularly in data-scarce settings or
29 exploratory studies. In this study, we explore the use of AEM for flow field uncertainty estimation,
30 with a particular focus on boundary uncertainty. To induce versatile, uncertain regional flow
31 more easily, we propose a new element based on conformal mapping. We then include this
32 element in a simple Python-based AEM toolbox and benchmark it against MODFLOW. Coupling
33 AEM with a Markov Chain Monte Carlo (MCMC) routine using adaptive proposals, we explore its
34 use in a synthetic case study. We find that AEM permits efficient uncertainty estimation for
35 groundwater flow fields, and its analytical nature readily permits continuing analyses which can
36 support Lagrangian transport modelling or the placement of numerical model boundaries.

37

38 1 Introduction

39 Groundwater modelling plays an important role in practical hydrogeology. In a discipline in which
40 neither the system nor its properties can be observed in its entirety, it is the task of models to
41 establish spatial and temporal continuity between point-wise information. Where only few
42 observations are available, uncertainty dominates the system characterization. These
43 uncertainties must be quantified to endow any information derived from models with the correct
44 confidence intervals.

45 Sources of model uncertainty are manifold and somewhat elusive, but arise from three main
46 sources: unknown subsurface parameters (parametric uncertainty: e.g., Linde et al. 2017; Renard
47 2007), unknown boundary conditions and forcings (forcing uncertainty: e.g., Guillaume et al.
48 2016; Vrugt et al. 2008), and model structural inadequacies (conceptual uncertainty; e.g., Höge,
49 Guthke, and Nowak 2019). In practice, hydrogeologists tend to devote most resources to
50 parametric uncertainty, focusing on the ambiguity in sediment parameters such as hydraulic
51 conductivity. Where forcing uncertainty is considered, it is rarely explored beyond the addition
52 of white noise to perturb model predictions. This omission can be problematic, since the
53 influence of forcing uncertainty may be indistinguishable from (e.g., Erdal and Cirpka 2016) or
54 even eclipse (e.g., Peeters and Turnadge 2019) the effects of parametric uncertainty.

55 While all models of unisolated systems require boundary conditions in some form, the specific
56 requirements depend on the chosen modelling framework. Numerical models place particularly
57 stringent requirements, demanding a finite domain along which specified boundary conditions
58 are enforced. Such boundaries are rarely well-defined in reality. Common pragmatic choices are

59 prescribed hydraulic head conditions inter- and extrapolated from marginal observation wells, or
60 no-flow boundaries along anticipated streamlines. Since the nature of these boundaries
61 intertwines them closely with the extent of the model grid, they do not lend themselves readily
62 to the exploration of uncertainty in their extent or nature without adjusting the grid as well.

63 Prescribed in- or outflow boundary conditions would be a more versatile choice to represent the
64 uncertain influence of regional flow in a finite domain, but are very difficult to inform and
65 consequently rarely used. Recognizing this limitation, simulation frameworks such as
66 MODFLOW 6 (Langevin et al. 2017) have since implemented multi-level setups which allow the
67 use of simpler, large-scale models to inform the flow boundaries of the main area of interest.
68 This shifts the boundary problem up the hierarchy, but at additional computational expense.

69 In search of a remedy, an interesting alternative may be found in the analytic element method
70 (AEM: Haitjema 1995; Strack 1989, 2017). Instead of discretizing the model domain into cells or
71 finite elements, AEM constructs a complex-valued, scale-invariant analytic solution to the flow
72 field. This is achieved through superposition (addition) of simpler solutions, the eponymous
73 analytic elements (Figure 1). While initially developed for two-dimensional, steady-state settings,
74 AEM has since been extended to support three-dimensional model domains (Haitjema 1985),
75 smooth inhomogeneities (Craig 2009), and transient dynamics (Furman and Neuman 2003). AEM
76 code has been distributed in modelling frameworks such as TIMML (Bakker 2006; Bakker and
77 Strack 2003), Visual AEM (Craig et al. 2009), or AnAqSim (Fitts et al. 2015).

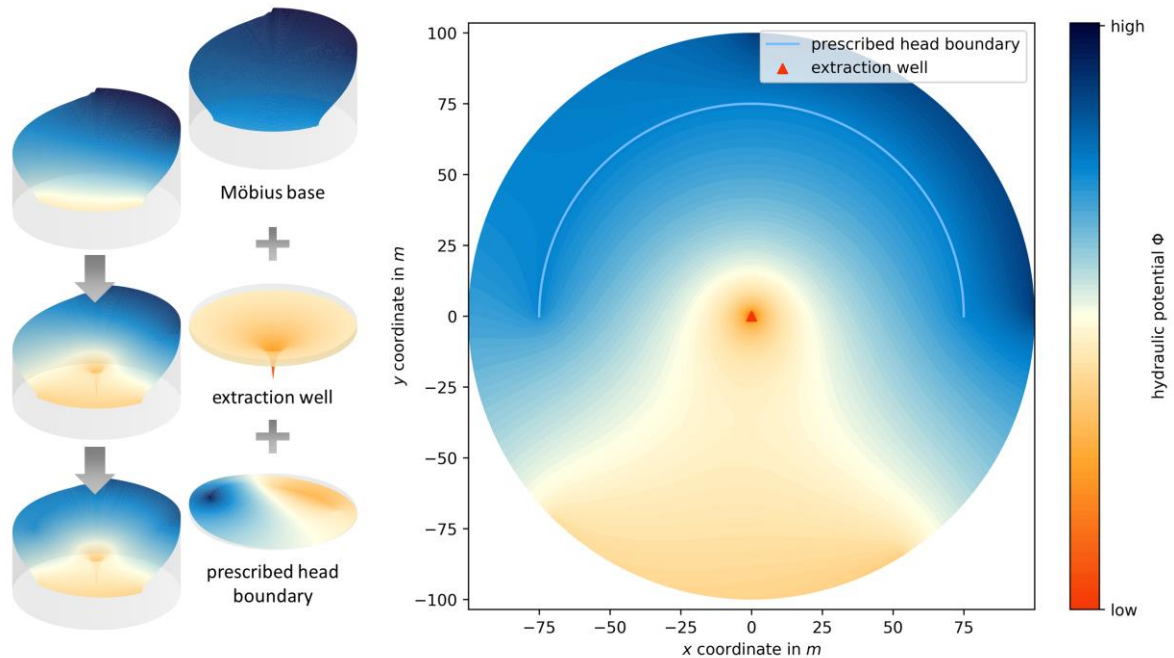


Figure 1. Example of how a AEM model is constructed. The influences of distinct elements (left) can be super-imposed to obtain a single, more complex solution (right, bottom left). Certain elements like prescribed head boundaries require additional preparation to ensure they induce the desired effect (see Section 2.1.8).

78 In the context of forcing uncertainty, AEM has the desirable property that it does not demand
 79 enclosure through finite, specified boundaries. Traditionally, regional flow is implemented as
 80 infinite, uniform flow, and subsequently deformed through the placement of farfield elements
 81 outside the immediate domain of interest. In principle, this method can induce highly complex
 82 flow fields, but is not very well suited for practical uncertainty estimation due to its indirect
 83 nature. More substantial changes to regional flow would require changing the position and
 84 rotation of the farfield elements.

85 In this study, our objective is two-fold: we strive to (i) demonstrate the intrinsic suitability of AEM
 86 for Bayesian inference, capitalizing on its naturally low parameter count and computational
 87 efficiency. Its natural approach to complexity (*start simple, add more complexity as required*) can
 88 make it more suitable for exploratory analyses than numerical models, which are often used the

89 other way around (*start complex, then simplify by aggregating grid parameters*). Towards this
90 end, we (ii) propose a new element based on a Möbius transformation, which can directly induce
91 curving, diverging, or converging regional base flow within a circular model domain of arbitrary
92 size. This improves AEM's suitability for the exploratory analysis of boundary uncertainty.

93 We subsequently demonstrate the use of AEM and this element for the inference of local, two-
94 dimensional, steady state flow fields. We provide a modular Python code coupling a simple AEM
95 implementation to a MCMC routine, intended for preliminary explorations of plausible flow fields
96 during model conceptualization, or simple Bayesian flow field inference in data-scarce
97 environments.

98 2 Theory

99 In this section, we will outline the basic concepts of AEM and some of the most common elements
100 (Section 2.1). The derivations summarized here are mainly based on and explored in much
101 greater detail in the seminal works of Otto Strack (1989, 2017). For our Python implementation,
102 we largely follow the object-oriented procedure suggested by Bakker & Kelson (2009). We
103 present the uncertainty estimation algorithm used in this study in Section 2.2. Variables in **bold**
104 notation denote vectors, matrices, or vector- or matrix-valued functions, while standard notation
105 is reserved for scalar-valued variables and functions. The derivatives of all elements presented in
106 the following are listed in Appendix 1 (supporting information).

107 2.1 Analytic Element Method

108 As opposed to conventional numerical models, the Analytic Element Method (AEM) does not
109 seek a solution in terms of hydraulic head, but instead computes a complex valued potential

$$\Omega = \Phi + i\Psi \quad (1)$$

110 where Φ is the *discharge (or hydraulic) potential*, Ψ is the *stream function*, which corresponds
 111 to the flow direction, and $i = \sqrt{-1}$ is the imaginary unit. At the heart of the method lies the
 112 superposition of simple linear differential equations – the eponymous analytic elements – to yield
 113 more intricate solutions:

$$\Omega = \sum_{e=1}^E f_e(\mathbf{z}; \theta_e) \quad (2)$$

114 where E is the number of analytic elements, and f_e is the function for a specific analytic element
 115 parameterized by θ_e and evaluated at \mathbf{z} , a vector of complex-valued coordinates:

$$\mathbf{z} = \mathbf{x} + i\mathbf{y}. \quad (3)$$

116 where \mathbf{x} and \mathbf{y} are two coordinate components. The conversion of hydraulic potential Φ into
 117 hydraulic heads ϕ depends on the aquifer type (Eq. 8.12 and 8.13, Strack 1989):

$$\phi = \frac{\Phi + \frac{1}{2}kH^2}{kH} \quad (\text{confined, } \Phi \geq \frac{1}{2}kH^2) \quad (4)$$

$$\phi = \sqrt{\frac{2\Phi}{k}} \quad (\text{unconfined, } \Phi < \frac{1}{2}kH^2) \quad (5)$$

118 where k is the hydraulic conductivity and H is the thickness of the aquifer. Its inverse is:

$$\Phi = kH\phi - \frac{1}{2}kH^2 \quad (\text{confined, } \phi \geq H) \quad (6)$$

$$\Phi = \frac{1}{2}k\phi^2 \quad (\text{unconfined, } \phi < H) \quad (7)$$

119 Analytic elements can be broadly classified into two groups. Some elements like extraction wells,
 120 line sinks, or area sinks only have to induce a *relative* change, for example extract a certain net
 121 amount of water. As such, they can simply be added to the stack and induce the desired flow

122 response. We will refer to such elements as *relative elements*. Other elements, like prescribed
 123 head boundary conditions, no-flow boundaries, or inhomogeneities must enforce an *absolute*
 124 condition at certain locations. These elements must adapt themselves to the influence of other
 125 elements. We will refer to such elements as *absolute elements*. The strength values of absolute
 126 elements can be found by setting up a system of linear equations, which we will describe in
 127 Section 2.1.8.

128 In the following, we will present a number of elements which will be used in this study. We will
 129 restrict our analysis to circular model domains, but note that all elements except the newly
 130 introduced Möbius base can operate on arbitrary – even infinite – domains.

131 2.1.1 Uniform base flow (relative)

132 Many analytic elements require some sort of background potential or base flow. A classic choice
 133 in AEM is uniform regional flow with specified direction, offset, and gradient:

$$\Omega = Qz \exp(-i\alpha) + \frac{\Phi_{min} + \Phi_{max}}{2} \quad (8)$$

$$Q = \frac{\Phi_{max} - \Phi_{min}}{2r_d} \quad (9)$$

134 where α is the flow's rotation in radians relative to the eastern axis, r_d is the radius of the circular
 135 domain, and Φ_{min} and Φ_{max} are the minimum and maximum discharge potential. These
 136 potentials can alternatively be obtained by defining a minimum and maximum hydraulic head
 137 ϕ_{min} and ϕ_{max} , then converting them to hydraulic potentials with Equation (6) or (7). The
 138 second right-hand side term in Equation (8) offset the potential to the range between Φ_{min} and
 139 Φ_{max} . An example of this flow is illustrated in Figure 2a.

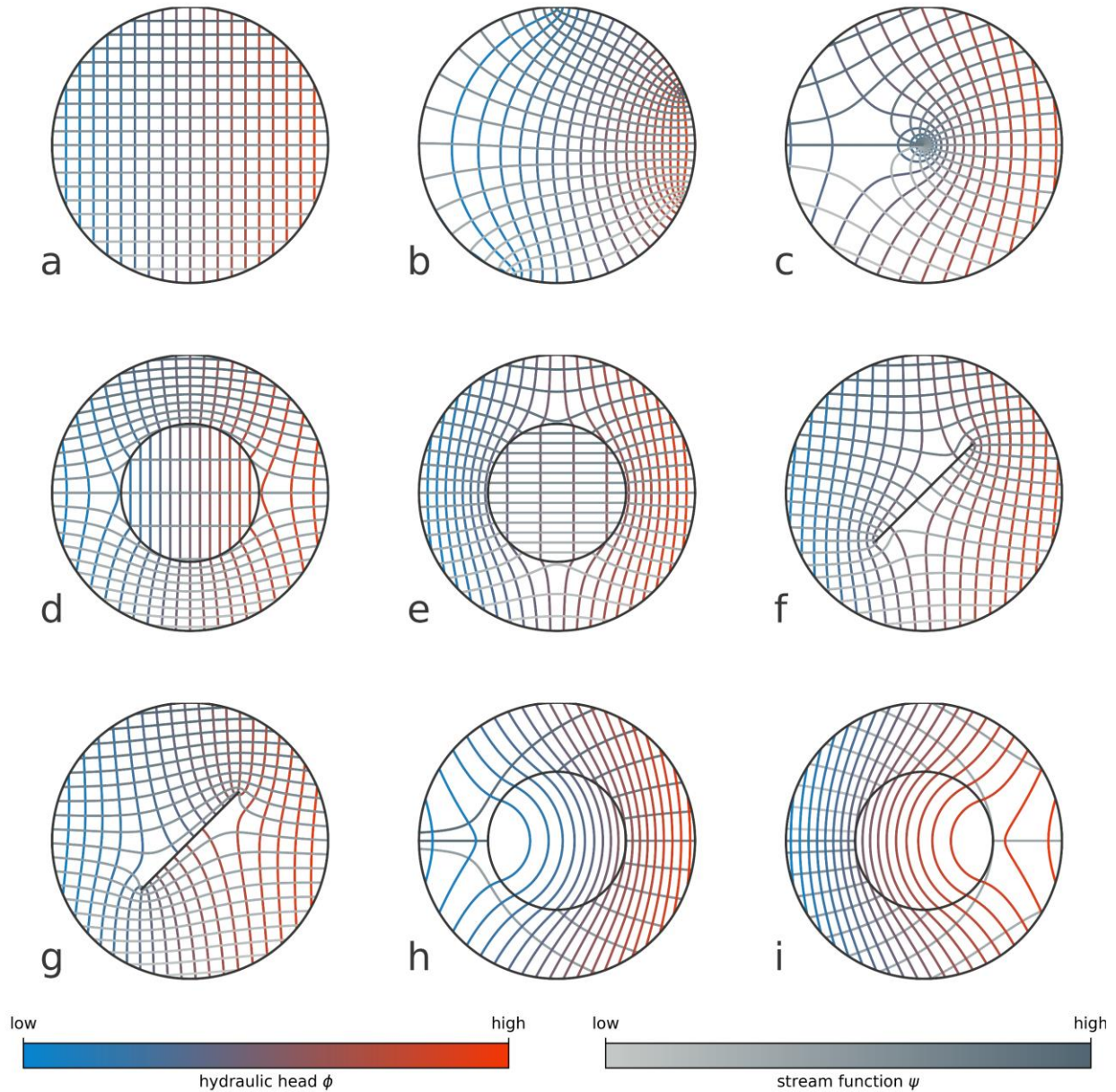


Figure 2. Various analytic elements used in this study. (a) uniform base flow, (b) Möbius base flow, (c) rate-specified extraction well, (d) polygonal inhomogeneity (lower), (e) polygonal inhomogeneity (higher), (f) prescribed head boundary, (g) no-flow boundary, (h) areal sink (negative), and (i) areal sink (positive). All elements are shown for confined conditions, and all elements from (c) onwards use uniform base flow. Solutions for the stream function are not valid inside areal sinks (h, i) and have been masked inside the element. Elements which add or remove water from the system (wells, line sinks, area sinks) induce branch cuts, discontinuities in the stream function from the element westwards.

140 2.1.2 Möbius base flow (relative)

141 Analytic elements can be superimposed on fields obtained from *conformal mapping* (e.g., Olver

142 2018). Conformal mapping is a class of angle-preserving transformations which can convert grids

143 in the complex plane – or, more specifically, simple complex potential fields such as flow on the

144 unit square from east to west – into more complex shapes, while preserving the validity of the
 145 solution. Classic example of such methods are Schwarz-Christoffel transformations (SC: e.g.,
 146 Driscoll and Trefethen 2009) and Möbius transformations.

147 To obtain more complex regional flow than the uniform flow defined in Section 2.1.1, we chain a
 148 Schwarz-Christoffel transformation with a Möbius transformation. First, the Schwarz-Christoffel
 149 transformation maps the unit square onto the unit disk. Then, the Möbius transformation
 150 deforms the flow inside the unit disk. This process is illustrated in Figure 3.

151 For computational purposes, we are mainly interested in the inverse of these maps: from the
 152 deformed unit disk (representing points in the model domain \mathbf{z} , Figure 3c) back onto the unit
 153 square (yielding the corresponding complex potential Ω , Figure 3a). The first step consists of
 154 casting the model domain back onto the unit disk through translation and scaling:

$$\mathbf{z}_{ud} = \frac{\mathbf{z} - z_d}{r_d} \quad (10)$$

155 where \mathbf{z} are coordinates in the model domain, z_d is the center and r_d the radius of the circular
 156 model domain. The inverse Möbius transformation is defined as:

$$\mathbf{A} = \mathbf{M}^{-1}(\mathbf{z}_{ud}; a, b, c, d) = \frac{-d\mathbf{z}_{ud} + b}{c - a} \quad (11)$$

157 where \mathbf{A} are the complex coordinates on the standard unit disk (Figure 3b), and $a, b, c,$ and d are
 158 the Möbius coefficients. These coefficients can be computed by defining three reference points
 159 on the standard unit circle (e.g., points A, B, and C in Figure 3b) and their *images* on the edge of
 160 the transformed Möbius unit disk (i.e., A, B, and C in Figure 3c). Instead of working with the
 161 complex-valued coordinates on the unit circle, it is easier to express them in terms of polar
 162 coordinates of unit length and angle φ :

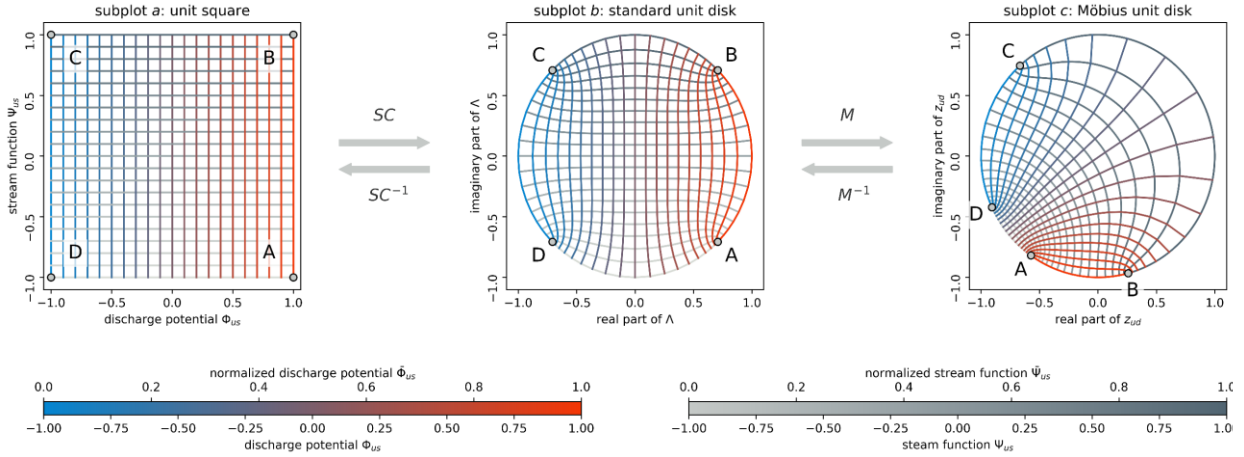


Figure 3. Illustration of the conformal mapping from the unit square (a) through the unit disk (b) to the Möbius-transformed unit disk (c). The control points A, B, and C in the unit disk (b) and the Möbius-transformed unit disk (c) define the coefficients for the Möbius transformation. The forward transformations SC and M are listed in Appendix 2.

$$Z_\varphi = P(\varphi) = \cos \varphi + i \sin \varphi \quad (12)$$

163 If we consider the static reference points in Figure 3b

$$\begin{aligned} A &:= \lambda_A = \cos(-0.25\pi) + i \sin(-0.25\pi) \\ B &:= \lambda_B = \cos(+0.25\pi) + i \sin(+0.25\pi) \\ C &:= \lambda_C = \cos(+0.75\pi) + i \sin(+0.75\pi) \end{aligned} \quad (13)$$

164 we can express their images on the Möbius unit circle of Figure 3c similarly

$$\begin{aligned} z_A &= \cos(\varphi_A) + i \sin(\varphi_A) \\ z_B &= \cos(\varphi_B) + i \sin(\varphi_B) \\ z_C &= \cos(\varphi_C) + i \sin(\varphi_C) \end{aligned} \quad (14)$$

165 Consequently, we can specify the Möbius transformation through three variables only: φ_A , φ_B ,

166 and φ_C . We can then calculate the desired Möbius coefficients:

$$\begin{bmatrix} a & b \\ c & d \end{bmatrix} = \begin{bmatrix} z_B - z_C & z_A z_C - z_A z_B \\ z_B - z_A & z_A z_C - z_C z_B \end{bmatrix}^{-1} \cdot \begin{bmatrix} \lambda_B - \lambda_C & \lambda_A \lambda_C - \lambda_A \lambda_B \\ \lambda_B - \lambda_A & \lambda_A \lambda_C - \lambda_C \lambda_B \end{bmatrix} \quad (15)$$

167 We may then map the standard unit disk onto the unit square with an inverse Schwarz-Christoffel

168 transformation (Fong 2019)

$$\Omega_{us} = \mathbf{S}\mathbf{C}^{-1}(\Lambda) = \frac{1-i}{-K_e} F\left(\mathbf{c} = \cos^{-1}\left(\frac{1+i}{\sqrt{2}}\Lambda\right), m = \frac{1}{\sqrt{2}}\right) + 1 - i \quad (16)$$

169 where Ω_{us} is the complex potential on the unit square, $F(\mathbf{c}, m)$ is the incomplete Legendre
 170 elliptical of the 1st kind with argument \mathbf{c} and parameter m :

$$F(\mathbf{c}, m) = \int_0^{\mathbf{c}} \frac{1}{\sqrt{1 - m \sin^2 t}} dt \quad (17)$$

171 and $K_e = F(\mathbf{c} = 0.5\pi, m = 0.5) \approx 1.854$. This transformation is illustrated in Figure 3a and b.
 172 Ω_{us} may then be transformed into a user-specified range:

$$\Omega = (\Phi_{max} - \Phi_{min}) (\Omega_{us} + 1)/2 + \Phi_{min} \quad (18)$$

173 A further examples of a Möbius base flow is shown in Figure 2b.

174 2.1.3 Extraction or injection wells (relative)

175 Wells are among the simplest analytic elements. The standard form of this element is (Equation
 176 24.8, Strack 1989):

$$\Omega = -\frac{Q}{2\pi} \ln(\mathbf{z} - z_{well}) + C \quad (19)$$

177 where Q is a positive or negative real-valued discharge, z_{well} is the location of the well in terms
 178 of complex coordinates, and C is a real constant. To recognize the need for the constant, consider
 179 the effect of the logarithm: If $\mathbf{z} = z_{well}$, the hydraulic potential is negative infinity, if
 180 $\|\mathbf{z} - z_{well}\| \rightarrow \infty$, the hydraulic potential approaches positive infinity.

181 This constant is usually combined with other additive constants in Equation (2) and determined
 182 by specifying a reference point of (assumed) known hydraulic potential in the so-called *farfield*,
 183 outside the area of interest. Defining this reference point is not a trivial task (Bakker et al. 2016;
 184 Haitjema 1995).

185 For practical purposes, we propose a slight adaptation. We adjust Equation (19) so that its
 186 influence on the discharge potential is zero at a distance of $\|z - z_{well}\| = r_i$ by subtracting the
 187 induced potential at this distance, which yields:

$$\Omega = -\frac{Q}{2\pi} (\ln(z - z_{well}) - \ln(r_i)) \quad (20)$$

188 where r_i is the radius at which we assume the induced drawdown to become zero. Outside the
 189 range of r_i , the hydraulic potential increases to positive infinity, so its value should be selected
 190 cautiously. By default, we set $r_i = 2r_d$. An example of this element is illustrated in Figure 2c.

191 2.1.4 Inhomogeneities (absolute)

192 As the subsurface can be heterogeneous, we may wish to create zones of piece-wise constant
 193 hydraulic conductivity. Towards this end, we can define zones of discontinuous hydraulic
 194 conductivity enclosed by a polygon:

$$\Omega = \sum_{j=1}^{N_j} \left[\frac{s_j}{4\pi i} \left((z_j + 1) \ln \left(\frac{z_j - 1}{z_j + 1} \right) - (z_{j+1} - 1) \ln \left(\frac{z_{j+1} - 1}{z_{j+1} + 1} \right) \right) \right] \quad (21)$$

195 Where N_j is the number of vertices spanning up the polygon, s_j are the strengths of each vertex,
 196 and

$$z_j = \frac{2z - (z_{j-1} + z_j)}{z_j - z_{j-1}} \quad (22)$$

197 where z_j is the j th vertex of a closed polygon, so that $z_0 = z_{N_j}$ and $z_{N_j+1} = z_1$. The vertices'
 198 strengths s_j are determined as part of the linear system (see Section 0) to enforce the desired
 199 discontinuity between the conductivity outside (k^-) and inside (k^+) the polygon. Examples for
 200 inhomogeneities of lower and higher conductivity are illustrated in Figure 2d and Figure 2e.

201 **2.1.5 Prescribed head boundaries (absolute)**

202 Line sinks inject or remove water along a line. As such, they can be used to simulate infiltration
 203 or exfiltration, for example from rivers, or to induce prescribed head boundaries. The extraction
 204 rate along a segment of the line element can be spatially varying (e.g., Janković and Barnes 1999;
 205 Strack 2018). In this study, we will use the constant rate formulation, and string together multiple
 206 *segments* of a line sink to implement spatially-varying extraction rates. Strack (1989) expresses
 207 the induced complex potential of line elements in terms of local coordinates:

$$\mathbf{Z} = \frac{2\mathbf{z} - (z_1 + z_2)}{z_2 - z_1} \quad (23)$$

208 where \mathbf{Z} is the local coordinate, \mathbf{z} the corresponding original coordinate, and z_1 and z_2 the
 209 original coordinates of the segment's start and end points. This is a small conformal mapping,
 210 projecting the line sink onto the real axis between -1 and $+1$, and transforming all evaluation
 211 points accordingly. Using these local coordinates, the induced potential is defined as (eq. 8.479,
 212 Strack 2017):

$$\Omega = s \frac{L}{4\pi} \left((\mathbf{Z} + 1) \ln(\mathbf{Z} + 1) - (\mathbf{Z} - 1) \ln(\mathbf{Z} - 1) + 2 \right) \quad (24)$$

213 where s is the strength of the line sink and $L = |z_2 - z_1|$ its length in global coordinates. Similarly
 214 to the well element, this element's induced hydraulic potential increases unbounded with
 215 distance. As a consequence, we subtract the effect an influence radius similarly to Section 2.1.3:

$$\Omega = s \frac{L}{4\pi} \left((\mathbf{Z} + 1) \ln(\mathbf{Z} + 1) - (\mathbf{Z} - 1) \ln(\mathbf{Z} - 1) - \left(\frac{2r_i}{L} + 2 \right) \ln \left(\frac{2r_i}{L} + 2 \right) + \left(\frac{2r_i}{L} \right) \ln \left(\frac{2r_i}{L} \right) \right) \quad (25)$$

216 where r_i is the distance of the zero influence point from the segment's end point in terms of
 217 global coordinates. This element can be used for prescribed head boundaries (as an absolute
 218 element) or as a specified flow line sink (as a relative element). We may further extend

219 Equation (25) by introducing a connectivity parameter $0 \leq c \leq 1$ to scale each segment's
 220 injection or extraction strength s after the linear system has been solved. A connectivity of 0
 221 means the flow field is unaffected by the prescribed head boundary, a connectivity of 1 implies
 222 the flow field is fully controlled at the prescribed head boundary. An example of this element is
 223 illustrated in Figure 2f.

224 2.1.6 No-flow boundaries (absolute)

225 Line doublets create discontinuities in the complex potential while maintaining the mass balance.

226 These elements can be used to create zonal inhomogeneities or no-flow boundaries. Their

227 complex potential influence can be derived as (Strack 1989):

$$\Omega = \frac{s}{4\pi i} \left((Z + 1) \ln \left(\frac{Z - 1}{Z + 1} \right) - (Z - 1) \ln \left(\frac{Z - 1}{Z + 1} \right) \right) \quad (26)$$

228 where s is the element's real-valued strength, and Z are localized coordinates of Equation (23).

229 No-flow boundaries are absolute elements and can be obtained by chaining together several such

230 segments in sequence. The no-flow condition is enforced by requiring that the gradient of the

231 hydraulic potential across each segment must be zero (see Section 0). An example of such an

232 element is illustrated in Figure 2g.

233 2.1.7 Area sinks (relative)

234 Area sinks are among the more complicated elements. Similar to inhomogeneities, they are

235 defined based on closed polygons (Eq. 8.598, Strack 2017):

$$\Omega = -\frac{Q}{32\pi i} \sum_{j=1}^{N_j} L_j^2 (Z_j - \bar{Z}_j) H(Z_j) + \frac{QA}{2\pi} \ln(z - z_1) \quad (27)$$

236 where Q is the designated flux rate per area, L_j is the length of the side from vertex $j - 1$ to j ,
 237 \mathbf{Z}_j is calculated according to Equation (22), $\bar{\mathbf{Z}}_j$ is its complex complement, A is the area enclosed
 238 by the polygon, and $\mathbf{H}(\mathbf{Z}_j)$ is calculated according to:

$$\mathbf{H}(\mathbf{Z}_j) = (\mathbf{Z}_j + 1) \ln \left(\frac{\mathbf{Z}_j - 1}{\mathbf{Z}_j + 1} \right) + 2 \sum_{m=j+1}^{N_j} \ln \left(\frac{\mathbf{Z}_m - 1}{\mathbf{Z}_m + 1} \right) + 2 \quad (28)$$

239 Examples of this element are illustrated in Figure 2h and Figure 2i.

240 2.1.8 Solving the system of linear equations

241 As we established in the beginning of Section 2.1, some elements must enforce absolute
 242 conditions at certain locations and thus depend on the influences of all other elements. To
 243 simultaneously satisfy the conditions imposed by these elements, their strengths s are estimated
 244 jointly as part of a linear system of equations (e.g., Bakker and Kelson 2009; Strack 1989):

$$\mathbf{A} \cdot \mathbf{s} = \mathbf{x} \quad (29)$$

245 where \mathbf{A} is a $N \times N$ matrix, N is the number of the absolute elements' line segments or polygon
 246 vertices, \mathbf{s} is a vector of length N containing all absolute segments' strength parameters s , and \mathbf{x}
 247 is a vector of length N specifying the conditions to be met.

248 To assemble \mathbf{A} , each entry of the n th row contains the influence of the other absolute elements
 249 on the n th absolute control point (the center of a line segment or a polygon vertex) at unit
 250 strength ($s = 1$). For segments of no-flow boundaries, each corresponding row is filled with the
 251 hydraulic potential gradient $\partial\Phi/\partial\mathbf{n}$ along the segment's normal vector \mathbf{n} . The required
 252 derivatives of all elements are reported in Appendix 1. For prescribed head boundaries and
 253 inhomogeneities, each row contains influences on the hydraulic potential Φ (Figure 4, Step 2). A
 254 special case applies for the diagonal entries corresponding to inhomogeneities. To these entries,

255 a term specifying the discontinuity of hydraulic conductivity is added ($k^-/(k^+ - k^-)$, see
 256 Section 2.1.4).

257 The target vector \mathbf{x} is assembled so that each absolute element's conditions are fulfilled:

- 258 • For *prescribed head boundaries*, the target hydraulic potential at the segment is
 259 calculated according to Equation (6) or (7), depending on aquifer type. Then, the Φ
 260 induced by the independent elements is subtracted from the target potential.
- 261 • For *no-flow boundaries*, the target is set to $-\partial\Phi/\partial\mathbf{n}$, the negative gradient induced by
 262 all relative elements on the segment (Figure 4, Step 3).
- 263 • For *inhomogeneities*, the target hydraulic potential at the vertex is set to the Φ induced
 264 by the independent elements times -1 .

265 With \mathbf{A} and \mathbf{x} defined, a standard linear solver can be used to obtain the unknown strength
 266 parameters \mathbf{s} .

267 2.2 Bayesian inference

268 Bayesian statistics are a formalized way of assigning probability densities, which can be
 269 interpreted as a plausibility metric, to different alternative hypotheses, often defined as a vector
 270 of unknown parameters $\boldsymbol{\theta} = [\theta_1, \dots, \theta_D]^\top$, where D is the number of uncertain parameters.
 271 When the number of hypotheses is infinite, for example in the case of continuous variables,
 272 Bayesian inference works with probability densities instead. These densities are defined through
 273 so-called *probability density functions (pdf)*. Bayes' Theorem formalizes the process of updating
 274 one's state of knowledge by combining initial belief – the prior $p(\boldsymbol{\theta})$ – with new information –
 275 the likelihood $p(\mathbf{y}|\boldsymbol{\theta})$ – to obtain the posterior pdf $p(\boldsymbol{\theta}|\mathbf{y})$ after normalization through the model
 276 evidence $p(\mathbf{y})$:

277 The prior is generally user-specified, and the likelihood is evaluated based on a user-defined
 278 function which specifies the probability of obtaining the observations made (\mathbf{y}) given the current

$$p(\boldsymbol{\theta}|\mathbf{y}) = \frac{p(\boldsymbol{\theta})p(\mathbf{y}|\boldsymbol{\theta})}{p(\mathbf{y})} \quad (30)$$

279

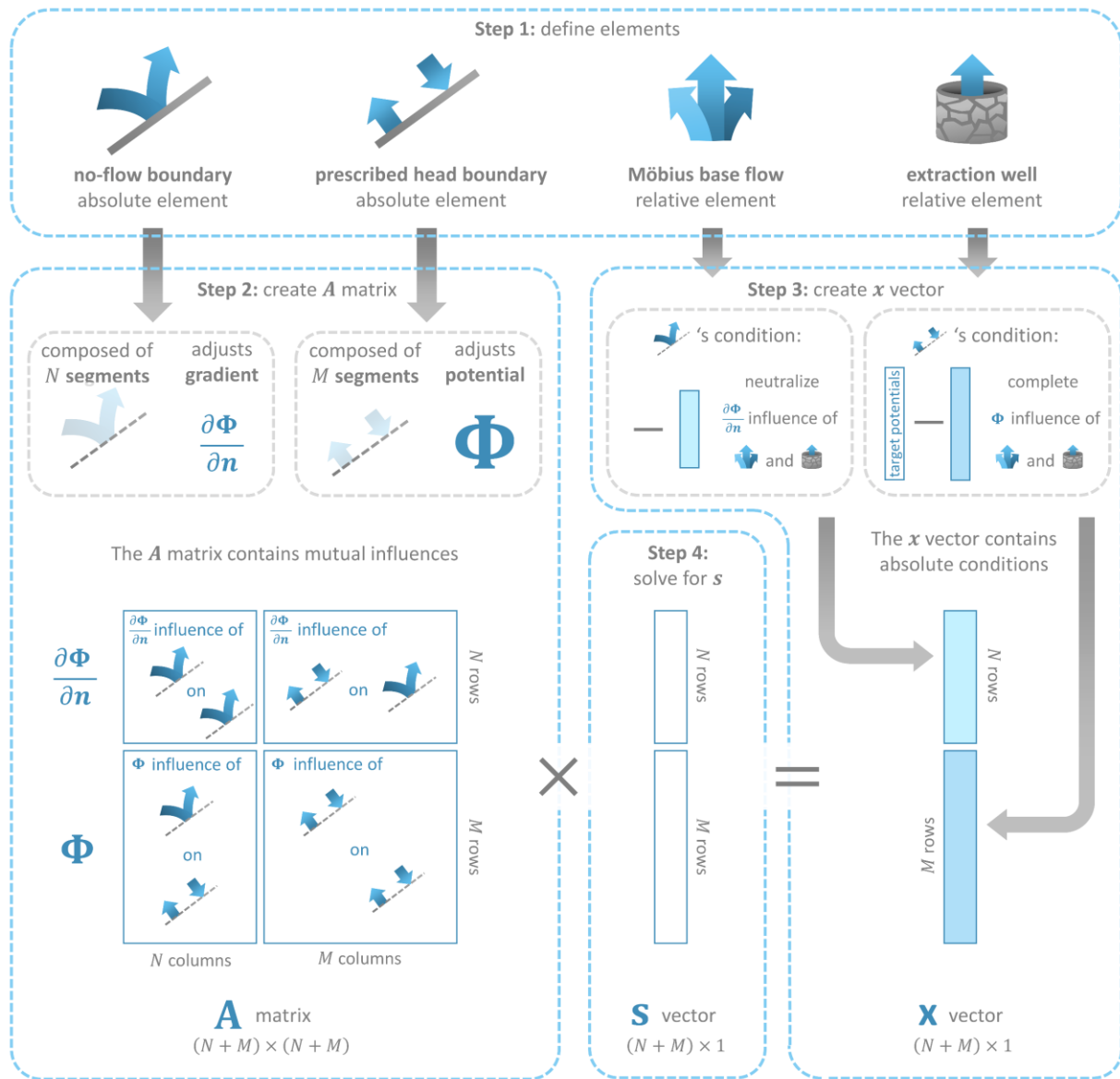


Figure 4. Schema for setting up the system of linear equations, illustrated in an example with two relative elements (Möbius base flow, extraction well) and two absolute elements (no-flow boundary, prescribed head boundary). After the elements are defined (Step 1), we create the \mathbf{A} matrix by specifying the mutual influences of the absolute elements' segments onto each other (Step 2). Similarly, we construct the target \mathbf{x} vector by evaluating and correcting the influence of the relative elements on the absolute elements' segments (Step 3). Finally, we can solve the linear system $\mathbf{A} \cdot \mathbf{s} = \mathbf{x}$ for \mathbf{s} (Step 4). In this figure, \mathbf{n} denotes a segment's normal vector, and \times denotes the dot product.

280 hypothesis θ . Unfortunately, it is generally impossible to solve Equation (30) analytically. The
 281 model evidence is rarely known, and it is not always possible to find a tractable analytic
 282 formulation for the posterior $p(\theta|\mathbf{y})$.

283 2.2.1 MCMC

284 However, even if Equation (30) does not have a closed form solution, inference methods such as
 285 MCMC can still *sample* from the unknown posterior (e.g., Kruschke 2015). This is useful because
 286 a sufficiently large sample set from a random distribution can act as a surrogate for the
 287 distribution itself, and consequently be used to infer its properties.

288 MCMC achieves this by starting from an initial hypothesis – the start point θ_0 – then exploring
 289 similar hypotheses nearby by sampling from a proposal distribution, exploring the
 290 neighbourhood of the current hypothesis. This proposal distribution can, for example, be

291 Gaussian:

$$\theta_{proposal} \sim \mathcal{N}(\theta_{k-1}, \Sigma) \quad (31)$$

292 where $\mathcal{N}(\boldsymbol{\mu}, \boldsymbol{\Sigma})$ defines a (possibly multivariate) normal distribution with mean $\boldsymbol{\mu} = \theta_{k-1}$ (the
 293 previous hypothesis) and (co)variance $\boldsymbol{\Sigma}$. ‘ \sim ’ represents ‘sampled from’, and the subscript k
 294 denotes the current iteration, or entry in the chain. MCMC then assembles a chain of samples by
 295 comparing each new hypothesis (the *proposal*) with the chain’s last entry (the *reference*), and
 296 accepts or rejects the proposal based on its unnormalized posterior density relative to the
 297 reference. If the proposal density is symmetric (it is equally probable to jump from the reference
 298 to the proposal than from the proposal to the reference), the acceptance probability p_{accept} can
 299 be calculated as:

$$p_{accept} = \min \left(1, \frac{p(\boldsymbol{\theta}_{proposal})p(\mathbf{y}|\boldsymbol{\theta}_{proposal})}{p(\boldsymbol{\theta}_{k-1})p(\mathbf{y}|\boldsymbol{\theta}_{k-1})} \right) \quad (32)$$

300 Equation (32) states that if the proposal is more plausible than the reference, the proposal is
 301 automatically accepted ($p_{accept} = 1$) and appended to the chain ($\boldsymbol{\theta}_k = \boldsymbol{\theta}_{proposal}$). If it is less
 302 plausible, it is either accepted with a probability equal to the posterior density ratio ($p_{accept} <$
 303 1) and appended to the chain ($\boldsymbol{\theta}_k = \boldsymbol{\theta}_{proposal}$), or rejected, in which case the reference is
 304 appended to the chain once more ($\boldsymbol{\theta}_k = \boldsymbol{\theta}_{k-1}$).

305 2.2.2 Adaptive proposals

306 A practical challenge in MCMC is that if the proposal distribution is sub-optimal, the chain will
 307 reject an inordinate amount of proposals, and consequently contain only very few unique
 308 samples. To avoid this issue, we implement our MCMC routine with an adaptive proposal
 309 distribution, gradually adjusting the proposal's covariance $\boldsymbol{\Sigma}$ so that a desired acceptance rate is
 310 achieved. Towards this end, we estimate an uncorrelated covariance matrix $\boldsymbol{\Sigma}_{unique}$ (i.e., all off-
 311 diagonal entries are set to zero) from the unique samples in the chain at regular intervals, then
 312 scale it with an adjustable factor f . The adjustable factor is increased if the acceptance rate was
 313 too high during the last interval, and decreased if it was too low:

$$\boldsymbol{\Sigma} = f\boldsymbol{\Sigma}_{unique} \quad (33)$$

314 Since it has been shown that adjustable proposals can corrupt the ergodic property, which is
 315 critical to the proper functioning of MCMC, it is important that the adjustments vanish
 316 asymptotically (e.g., Andrieu and Thoms 2008). For $\boldsymbol{\Sigma}_{unique}$ this should occur automatically as
 317 the number of samples increases, and for the adjustable factor f we achieve this by reducing the
 318 magnitude of its update exponentially:

$$f_c = f_{c-1} \left(a^{-c} \left(\frac{ratio_{accepted}}{ratio_{target}} - 1 \right) + 1 \right) \quad (34)$$

319 where $a > 1$ is a scalar which defines the speed of the decay, c is the current adjustment cycle,
 320 $ratio_{accepted}$ the percentage of accepted proposals since the last iteration, and $ratio_{target}$ the
 321 desired percentage of accepted proposals.

322 3 Examples

323 In this section, we illustrate the performance of the algorithm for two test cases. For the first test
 324 case, we benchmark our Python AEM code against MODFLOW, a well-established numerical
 325 finite-volume (FVM) framework. In the second test case, we demonstrate the performance of the
 326 AEM model and the MCMC inference mechanism in a synthetic test case. **The codes for both**
 327 **scenarios are provided under a DOI which does not yet exist, see acknowledgements.**

328 3.1 Benchmarking

329 For benchmarking, we compare the results from our Python AEM implementation to the results
 330 of a steady-state MODFLOW 6 model (Bakker et al. 2016; Langevin et al. 2017) at varying grid
 331 resolutions. Towards this end, we design a simple synthetic model employing every element
 332 described in Section 2.1 except the base flow elements (uniform or Möbius), as they are
 333 redundant in a domain enclosed by absolute boundaries (a prerequisite of the numerical
 334 reference). A schematic illustration of the benchmarking model is illustrated in Figure 5a, and the
 335 results compared to different resolutions of uniformly-sized hexagonal grids are shown in Figure
 336 5b-d.

337 The results indicate that our AEM code can faithfully reproduce the FVM predictions, and that
 338 conversely the FVM results converge towards the AEM solution at finer grid sizes. This is mainly

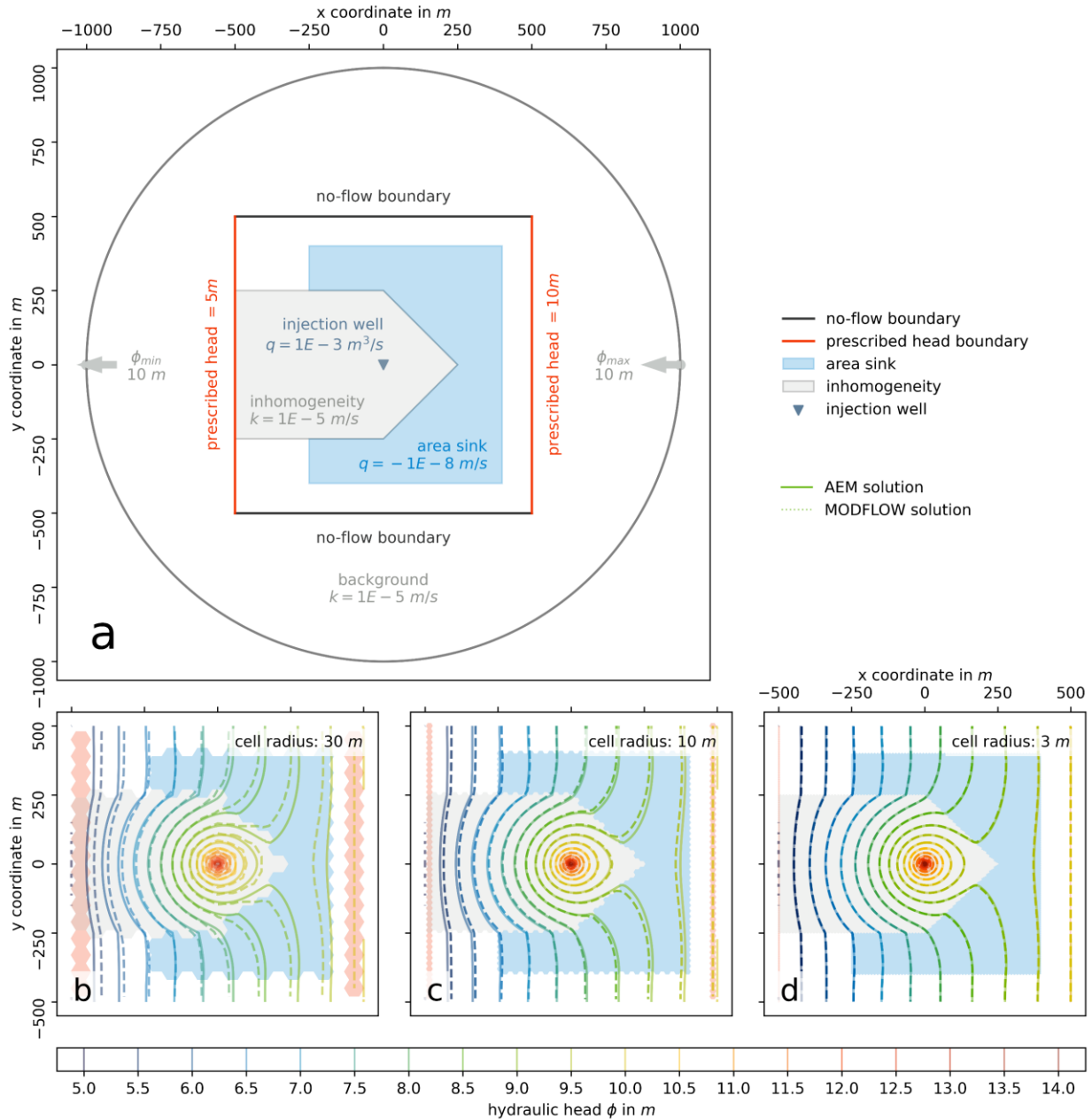


Figure 5. Illustrations of the benchmarking test case. To define a system which can be equivalently evaluated numerically, we embed a square area enclosed by two no-flow and two prescribed head boundaries within (functionally irrelevant) uniform flow. The model domain includes an area sink, an inhomogeneity, and an injection well (a). We compare the AEM results (solid line; b, c, d) with three FVM grids of different cell sizes (dashed line): 30 m (b), 10 m (c), and 3 m (d). The finer the cell resolution, the more the FVM results converge towards the AEM solution. The discrepancies arise because numerical grid sizes determine how well flow-relevant features can be resolved.

339 owed to the inability of rougher grid sizes to reproduce the boundaries and features in Figure 5a

340 as faithfully as finer resolutions. We do however note that unstructured grids – which may adopt

341 the cell size and shape locally to reproduce features more precisely – can yield solutions closer
342 to AEM more efficiently than the uniform regular grids shown here.

343 3.2 Synthetic test case

344 To illustrate the potential of AEM for practical groundwater field inference, we apply the
345 algorithm in a synthetic test case. Revisiting the motivating issue of uncertain boundary
346 conditions, we design our synthetic site as local part of a larger catchment, with limited head
347 information and poorly defined boundary conditions. Such scenarios abound in hydrogeological
348 practice.

349 The water table is assumed to be observed at an extraction well and three surrounding
350 observation wells (Figure 6a). Towards the north-west, a river of unknown connectivity intersects
351 the domain. This river is implemented as a prescribed head boundary with four support nodes
352 for the interpolation of the river's connectivity. The river is embedded in an inhomogeneity of
353 unknown hydraulic conductivity. In the south, we prescribe a no-flow boundary representing an
354 impermeable geological formation.

355 We define priors centered around the true solution (Table S1, supporting information),
356 independent Gaussian observation errors ($\mu = 0\text{m}$, $\sigma = 0.15\text{m}$), and a MCMC chain length of
357 10,000. The original proposal distribution is listed in Table S2 (supporting information).

358 The results are illustrated in (Figure 6b-d). The RMSE (0.021 m) and bias (-0.004 m) reflect the
359 model's lack of structural error, but a glance at its uncertainty (Figure 6c) reveals the ambiguity
360 in the system's states. Uncertainty in the groundwater field is lowest between the observation
361 wells, then swiftly increases towards the domain's edges.

362 Although this synthetic scenario is somewhat simplistic, we can illustrate some of the potential
363 of AEM beyond simple groundwater field inference. Figure 6d illustrates a selection of uncertain

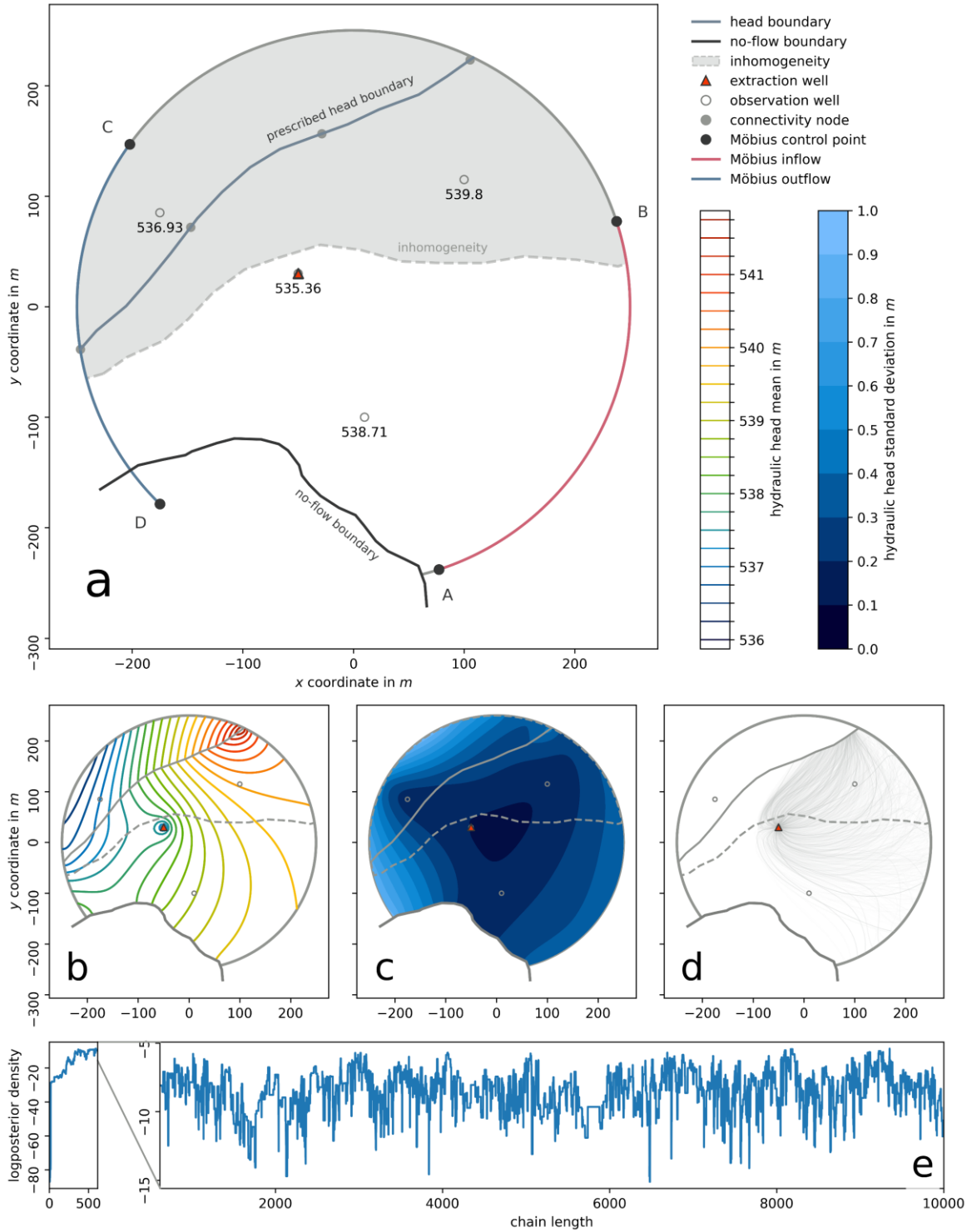


Figure 6. Schematic illustration (a) and results (b, c, d, e) for the synthetic test case. The model is implemented on a Möbius base with an areal inhomogeneity, an extraction well, a prescribed head boundary with spatially interpolated connectivity, and a no-flow boundary. Hydraulic heads are observed at three observation wells and the pumping well. Subplots (b) and (c) show the posterior mean and standard deviation of hydraulic head. Subplot (d) shows a selection of pathlines towards the extraction well. Subplot (e) shows the proportional logposterior density (right) and its cutoff (left) of the MCMC.

364 flow paths towards the extraction well, which may serve as the basis for Lagrangian transport
 365 modelling. Similarly, we could investigate the sign and magnitude of the river segments' strength
 366 values to obtain probabilistic estimates about which parts of the river are losing or gaining.

367 Using the algorithm as a support tool for model conceptualization, we can explore its use for the
 368 assignment of numerical model boundaries. This transition to numerical models might be
 369 motivated by Eulerian transport simulations or the investigation of transient dynamics.

370 Naturally, it would be possible to calculate regional fluxes based on the AEM predictions and
 371 assign these as inflow or outflow boundaries. For transient dynamics, however, the user might
 372 wish to return to no-flow boundaries and time-variable prescribed head boundaries, which are
 373 more easily informed through marginal observation wells. If the observations and priors for the
 374 steady state AEM simulation were sufficiently representative of the average dynamics, either
 375 boundary type is best assigned in regions where the posterior AEM flow direction is relatively
 376 certain (deep blue regions in Figure 7).

377 The map in Figure 7 can be obtained by capitalizing on AEM's analytical nature to directly
 378 evaluate the hydraulic potential gradient $\frac{\partial\Phi}{\partial z}$ for each entry in the MCMC chain. The resulting set

379 of gradients at each individual location $z \in \mathbf{z}$ can be converted to a set of flow directions $\alpha =$

380 $\text{atan2}\left(x = \Re\left(\frac{\partial\Phi}{\partial z}\right), y = \Im\left(\frac{\partial\Phi}{\partial z}\right)\right)$, where $\Re(\cdot)$ and $\Im(\cdot)$ are the real and imaginary components

381 of their respective arguments. Since the direction of flow it is irrelevant for the assignment of

382 boundaries (i.e., $\alpha = -0.25\pi \triangleq 0.75\pi$), we can furthermore offset all angles $\alpha < 0$ by π to

383 obtain a more concise estimate, assuming $-\pi \geq \alpha > \pi$. If we then calculate the circular standard

384 deviation for each α , we obtain the contours in Figure 7. Prescribed head boundaries with

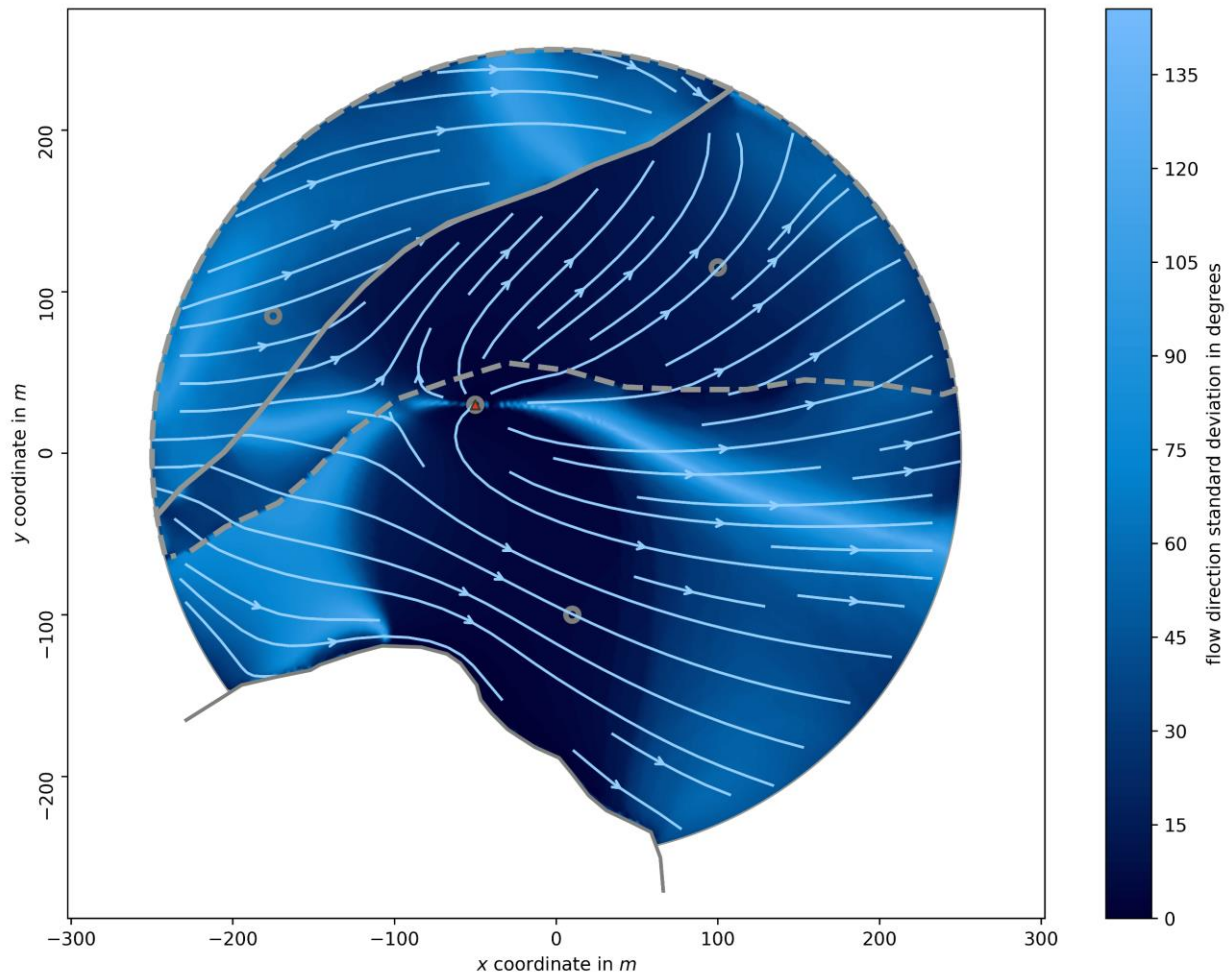


Figure 7. Posterior circular mean (streamlines) and circular standard deviation (filled contours) of the hydraulic potential gradient direction. For the purpose of assigning no-flow boundaries, each direction and its opposite are identical (i.e., $0.5\pi \triangleq -0.5\pi$). Consequently, we estimated the circular standard deviation of the flow direction angles, with all negative angles offset by 180 degrees.

385 constant head are best assigned perpendicular to the flow lines (light blue). No-flow boundaries

386 are best assigned parallel to the flow lines.

387 4 Discussion and Conclusions

388 In this study, we explored the use of the AEM for the inference of uncertain groundwater tables,

389 particularly under the lens of uncertain regional flow. Towards this end, we expanded the

390 standard toolbox of analytical elements with an element based on conformal mapping. This new

391 element flexibly induces curving, converging, or diverging regional flow in a circular model

392 domain of arbitrary size. We subsequently benchmarked our toolbox against a numerical model
393 (MODFLOW 6) for varying grid resolutions.

394 To examine the performance of the toolbox in practice, we explored its application in a simple
395 synthetic scenario. Coupling the model to an MCMC routine, we sampled from its parameter
396 posterior and simulated the corresponding uncertain groundwater flow fields. Finally, we
397 illustrated a few possible analyses of the inferred water tables: water table uncertainty, simple
398 pathline tracing, or decision support for the placement of numerical model boundaries.

399 We find that AEM can be a computationally efficient tool for the exploration of uncertain flow
400 fields in data-scarce environments. Its comparatively simple structure and consequently
401 straightforward uncertainty estimation can make it attractive for the estimation of probabilistic
402 flow maps, particularly in studies without a primary focus on subsurface characterization.
403 Alternatively, it can prove valuable as a support tool in preparation for more complex numerical
404 models, particularly the assignment of boundaries.

405 In summary, we believe that AEM constitutes a highly attractive compromise between simplistic,
406 often one-dimensional analytical groundwater flow solutions (e.g., method of fragments: Harr
407 2006), and the sometimes debilitating complexity of full numerical models. Its usually low
408 parameter count and high computational efficiency renders AEM naturally well-suited for most
409 Bayesian uncertainty estimation methods. In light of the push towards more comprehensive
410 uncertainty analyses over the past decades, we remain confident that this property in particular
411 warrants greater attention to AEM in the future. We have provided the AEM and MCMC
412 toolboxes used in this study in the supporting information and on GitHub under
413 <https://maxramgraber.github.io/Simple-AEM-Toolbox/>.

414 5 Acknowledgements

415 We express our gratitude to Prof. Otto Strack, University of Minnesota, and Prof. James Craig,
416 University of Waterloo, who answered our questions about AEM at different points during the
417 preparation of the manuscript. We are also indebted to Prof. Mark Bakker, Delft University of
418 Technology, for clarifying our understanding of the farfield reference point during the
419 preparation of the manuscript. The research leading to these results has received funding from
420 the European Union's Horizon 2020 research and innovation programme under the Marie
421 Skłodowska-Curie grant agreement No 675120. The data and algorithms to reproduce the results
422 reported in this study have been uploaded under a DOI which does not yet exist. Instead, we
423 have temporarily uploaded all files as a zipped folder under
424 <https://drive.switch.ch/index.php/s/nnkqbNHqnroWwvd>.

425

426 **References**

- 427 Andrieu, Christophe, and Johannes Thoms. 2008. "A Tutorial on Adaptive MCMC." *Statistics and*
428 *Computing*. doi: 10.1007/s11222-008-9110-y.
- 429 Bakker, M., V. Post, C. D. Langevin, J. D. Hughes, J. T. White, J. J. Starn, and M. N. Fienen. 2016.
430 "Scripting MODFLOW Model Development Using Python and FloPy." *Groundwater*
431 54(5):733–39. doi: 10.1111/gwat.12413.
- 432 Bakker, Mark. 2006. "An Analytic Element Approach for Modeling Polygonal Inhomogeneities in
433 Multi-Aquifer Systems." *Advances in Water Resources*. doi:
434 10.1016/j.advwatres.2005.11.005.
- 435 Bakker, Mark, and Victor A. Kelson. 2009. "Writing Analytic Element Programs in Python."
436 *Ground Water*. doi: 10.1111/j.1745-6584.2009.00583.x.
- 437 Bakker, Mark, and Otto D. L. Strack. 2003. "Analytic Elements for Multiaquifer Flow." *Journal of*
438 *Hydrology*. doi: 10.1016/S0022-1694(02)00319-0.
- 439 Craig, J., I. Janković, M. Bakker, and S. Matott. 2009. "Visual AEM."
- 440 Craig, J. R. 2009. "Analytic Elements for Flow in Harmonically Heterogeneous Aquifers." *Water*
441 *Resources Research* 45(6). doi: 10.1029/2009WR007800.
- 442 Driscoll, Tobin A., and Lloyd N. Trefethen. 2009. *Schwarz-Christoffel Mapping*. Cambridge
443 University Press.
- 444 Erdal, D., and O. A. Cirpka. 2016. "Joint Inference of Groundwater‐Recharge and
445 Hydraulic‐Conductivity Fields from Head Data Using the Ensemble Kalman Filter."

- 446 *Hydrology and Earth System Sciences*. doi: 10.5194/hess-20-555-2016.
- 447 Fitts, Charles R., Joshua Godwin, Kathleen Feiner, Charles Mclane, and Seth Mullendore. 2015.
- 448 “Analytic Element Modeling of Steady Interface Flow in Multilayer Aquifers Using
- 449 AnAqSim.” *Groundwater*. doi: 10.1111/gwat.12225.
- 450 Fong, Chamberlain. 2019. “Analytical Methods for Squaring the Disc.” *ArXiv Preprint*
- 451 *ArXiv:1509.06344*.
- 452 Furman, Alex, and Shlomo P. Neuman. 2003. “Laplace-Transform Analytic Element Solution of
- 453 Transient Flow in Porous Media.” *Advances in Water Resources*. doi:
- 454 10.1016/j.advwatres.2003.09.003.
- 455 Guillaume, Joseph H. A., Randall J. Hunt, Alessandro Comunian, Rachel S. Blakers, and Baihua
- 456 Fu. 2016. “Methods for Exploring Uncertainty in Groundwater Management Predictions.”
- 457 in *Integrated Groundwater Management: Concepts, Approaches and Challenges*.
- 458 Haitjema, H. M. 1985. “Modeling Three-Dimensional Flow in Confined Aquifers by
- 459 Superposition of Both Two- and Three-Dimensional Analytic Functions.” *Water Resources*
- 460 *Research*. doi: 10.1029/WR021i010p01557.
- 461 Haitjema, H. M. 1995. “Analytic Element Modeling.” in *Analytic Element Modeling of*
- 462 *Groundwater Flow*.
- 463 Harr, Milton. 2006. “Groundwater and Seepage.” in *The Handbook of Groundwater Engineering,*
- 464 *Second Edition*.
- 465 Höge, M., A. Guthke, and W. Nowak. 2019. “The Hydrologist’s Guide to Bayesian Model

- 466 Selection, Averaging and Combination.” *Journal of Hydrology*.
- 467 Janković, I., and R. Barnes. 1999. “High-Order Line Elements in Modeling Two-Dimensional
468 Groundwater Flow.” *Journal of Hydrology*. doi: 10.1016/S0022-1694(99)00140-7.
- 469 Kruschke, John. 2015. *Doing Bayesian Data Analysis: A Tutorial Introduction with R JAGS, and*
470 *Stan*.
- 471 Langevin, Christian D., Joseph D. Hughes, E. R. Banta, Richard G. Niswonger, Sorab Panday, and
472 A. M. Provost. 2017. “Documentation for the MODFLOW 6 Groundwater Flow Model.” *U.S.*
473 *Geological Survey*. doi: 10.3133/tm6A55.
- 474 Linde, Niklas, David Ginsbourger, James Irving, Fabio Nobile, and Arnaud Doucet. 2017. “On
475 Uncertainty Quantification in Hydrogeology and Hydrogeophysics.” *Advances in Water*
476 *Resources*. doi: 10.1016/j.advwatres.2017.10.014.
- 477 Olver, Peter J. 2018. “Complex Analysis and Conformal Mapping.” 84.
- 478 Peeters, L. J. M., and C. Turnadge. 2019. “When to Account for Boundary Conditions in
479 Estimating Hydraulic Properties from Head Observations?” *Groundwater*.
- 480 Renard, Philippe. 2007. “Stochastic Hydrogeology: What Professionals Really Need?” *Ground*
481 *Water*. doi: 10.1111/j.1745-6584.2007.00340.x.
- 482 Strack, O. D. L. 2018. “Limitless Analytic Elements.” *Water Resources Research*. doi:
483 10.1002/2017WR022117.
- 484 Strack, Otto D. L. 1989. *Groundwater Mechanics*. New Jersey: Prentice-Hall, Inc.
- 485 Strack, Otto D. L. 2017. *Analytical Groundwater Mechanics*. 1st ed. Cambridge University Press.

486 Vrugt, Jasper A., Cajo J. F. ter Braak, Martyn P. Clark, James M. Hyman, and Bruce A. Robinson.
487 2008. "Treatment of Input Uncertainty in Hydrologic Modeling: Doing Hydrology Backward
488 with Markov Chain Monte Carlo Simulation." *Water Resources Research*. doi:
489 10.1029/2007wr006720.
490